

# Seasonal Variability of Thermohaline Front in the Central South China Sea

PETER C. CHU<sup>1\*</sup> and WANG GUIHUA<sup>2</sup>

<sup>1</sup>Department of Oceanography, Naval Postgraduate School, Monterey, CA 93943, U.S.A.

<sup>2</sup>Laboratory of Ocean Dynamic Processes & Satellite Oceanography, Second Institute of Oceanography, State Oceanic Administration, Hangzhou 310012, China

(Received 22 November 2001; in revised form 13 May 2002; accepted 14 May 2002)

**An upper layer thermohaline front across the South China Sea (SCS) basin from the South Vietnamese coast (around 15°N) to Luzon Island (around 19°N) has been identified using the Navy's open domain Generalized Digital Environmental Model (GDEM) monthly mean temperature and salinity data on a  $0.5^\circ \times 0.5^\circ$  grid. This front does not occur at the surface in summer. The strength of this front is around  $1^\circ\text{C}/100$  km at the surface and  $1.4^\circ\text{C}/100$  km at the subsurface (50 m deep). A cross-basin current, inverted using the P-vector method, is associating with the front. Meandering and eddies have been identified along this current. Seasonal and vertical variabilities of the thermohaline structure across this front are reported in this paper.**

Keywords:

- Thermohaline front,
- South China Sea,
- P-vector method,
- meandering,
- eddies.

## 1. Introduction

The South China Sea (SCS) has a bottom topography (Fig. 1) that makes it a unique, semi-enclosed ocean basin that is temporally forced by a pronounced monsoon wind. Extended continental shelves (less than 100 m deep) exist along the north boundary and across the southwest portion of the basin, while steep slopes with almost no shelf are found along the eastern boundary. The deepest water is confined to an oblate bowl oriented SW-NE, centered around 13°N. The maximum depth is around 4500 m. The main connection between the SCS and the Pacific Ocean is via the Luzon Strait, which is very wide and has a sill depth of approximately 2400 m.

Analyzing historical hydrographic data over a wide region of the northern SCS, Shaw (1989, 1991) found an evident intrusion current from the Philippine Sea over a wide region of the northern SCS in late autumn and winter. Using a high-resolution Navy layered ocean model, Metzger and Hurlburt (1996, 2001) investigated the dynamics of the flow from the Pacific Ocean into the SCS. The Kuroshio intrusion into the SCS through the Luzon Strait is an important process, influencing the hydrographic features and circulation pattern in the north SCS (Nitani, 1970; Shaw, 1989, 1991; Chao *et al.*, 1996; Li *et al.*, 1998; Chu *et al.*, 1999). Such a process might

cause the observed difference in water mass characteristics between north and south SCS.

NASA's Multi-Channel Sea Surface Temperature (MCSST) data clearly show the appearance of a cross basin, thermal front in the winter (Fig. 2(a)) and disappearance of such a front in the summer (Fig. 2(b)). The frontal feature identified in Fig. 2(a) is a surface phenomenon. What is the three dimensional structure of the front? What are the water mass characteristics across the front? What is the current structure associated with the front? We have investigated these questions in this study using the Navy's Generalized Digital Environmental Model (GDEM) climatological temperature and salinity data on a  $0.5^\circ \times 0.5^\circ$  grid.

The outline of the paper is as follows. Section 2 depicts seasonal variability of surface winds. Section 3 describes the Navy's GDEM data set. Section 4 delineates the existence of a cross-basin thermohaline front. Section 5 depicts the identification of a cross-basin current associating with the thermohaline front using the P-vector inverse method. Section 6 describes the change of water mass characteristics across the thermohaline front. Section 7 presents the conclusions.

## 2. Seasonal Variability of Surface Winds

SCS experiences two monsoons, winter and summer, every year. During the winter monsoon season, a cold northeast wind blows over SCS (Fig. 3(a)) as a result of the Siberian high pressure system located over the east

\* Corresponding author. E-mail: chu@nps.navy.mil

Report Documentation Page			Form Approved OMB No. 0704-0188		
Public reporting burden for the collection of information is estimated to average 1 hour per response, including the time for reviewing instructions, searching existing data sources, gathering and maintaining the data needed, and completing and reviewing the collection of information. Send comments regarding this burden estimate or any other aspect of this collection of information, including suggestions for reducing this burden, to Washington Headquarters Services, Directorate for Information Operations and Reports, 1215 Jefferson Davis Highway, Suite 1204, Arlington VA 22202-4302. Respondents should be aware that notwithstanding any other provision of law, no person shall be subject to a penalty for failing to comply with a collection of information if it does not display a currently valid OMB control number.					
1. REPORT DATE <b>2003</b>		2. REPORT TYPE		3. DATES COVERED <b>00-00-2003 to 00-00-2003</b>	
4. TITLE AND SUBTITLE <b>Seasonal Variability of Thermohaline Front in the Central South China Sea</b>			5a. CONTRACT NUMBER		
			5b. GRANT NUMBER		
			5c. PROGRAM ELEMENT NUMBER		
6. AUTHOR(S)			5d. PROJECT NUMBER		
			5e. TASK NUMBER		
			5f. WORK UNIT NUMBER		
7. PERFORMING ORGANIZATION NAME(S) AND ADDRESS(ES) <b>Naval Postgraduate School,833 Dyer Road,Monterey,CA,93943</b>			8. PERFORMING ORGANIZATION REPORT NUMBER		
9. SPONSORING/MONITORING AGENCY NAME(S) AND ADDRESS(ES)			10. SPONSOR/MONITOR'S ACRONYM(S)		
			11. SPONSOR/MONITOR'S REPORT NUMBER(S)		
12. DISTRIBUTION/AVAILABILITY STATEMENT <b>Approved for public release; distribution unlimited</b>					
13. SUPPLEMENTARY NOTES					
14. ABSTRACT <b>See Report</b>					
15. SUBJECT TERMS					
16. SECURITY CLASSIFICATION OF:			17. LIMITATION OF ABSTRACT <b>Same as Report (SAR)</b>	18. NUMBER OF PAGES <b>14</b>	19a. NAME OF RESPONSIBLE PERSON
a. REPORT <b>unclassified</b>	b. ABSTRACT <b>unclassified</b>	c. THIS PAGE <b>unclassified</b>			

Asian continent. Radiative cooling and persistent cold air advection maintain cold air over SCS. The northeast-southwest oriented jet stream is positioned at the central SCS. Such a typical winter monsoon pattern lasts nearly

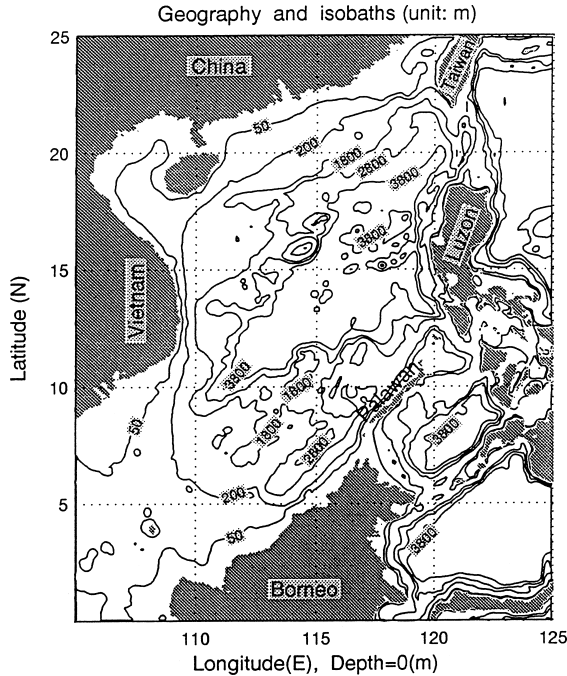


Fig. 1. Geography and isobaths showing the bottom topography of the South China Sea.

six months (November to April). During the summer monsoon season, a warm and weaker southwest wind blows over SCS (Fig. 3(b)). Such a typical summer monsoon pattern lasts nearly 4 months (mid-May to mid-September). The mean surface wind stress over SCS is nearly  $0.2 \text{ N/m}^2$  and reaches  $0.3 \text{ N/m}^2$  in the central portion in December (Fig. 3(a)) and is nearly  $0.1 \text{ N/m}^2$  in June (Fig. 3(b)).

The surface wind stress curl ( $\zeta$ ) field was calculated using the European Centre for Medium-Range Weather Forecast (ECMWF) analyzed wind data. The ensemble mean (1982–1989)  $\zeta$  field (Fig. 4(a)) shows a dipole pattern (Chu *et al.*, 1997b) with a northeast-to-southwest oriented zero-curl contour separating the SCS into cyclonic (anticyclonic) curls southeastern (northwestern) of it. The maximum absolute values of both curls reach  $1.8\text{--}2 \times 10^{-7} \text{ N/m}^3$ . The zero-curl contour represents the location of a prevailing southwestward surface jet stream.

During the winter monsoon season, the dipole pattern of the  $\zeta$  field (January) is similar to the ensemble mean pattern (Fig. 4(b)). Such a pattern persists from November to March. The maximum absolute values of both curls in January reach  $4 \times 10^{-7} \text{ N/m}^3$ , which implies a strong southwestward surface jet located at the zero-curl line.

During the summer monsoon season, the dipole pattern of the  $\zeta$  field (July) is opposite to the winter (or ensemble mean) pattern (Fig. 4(c)) with a northeast-to-southwest oriented zero-curl contour separating the SCS into anticyclonic (cyclonic) curls southeast (northwest)

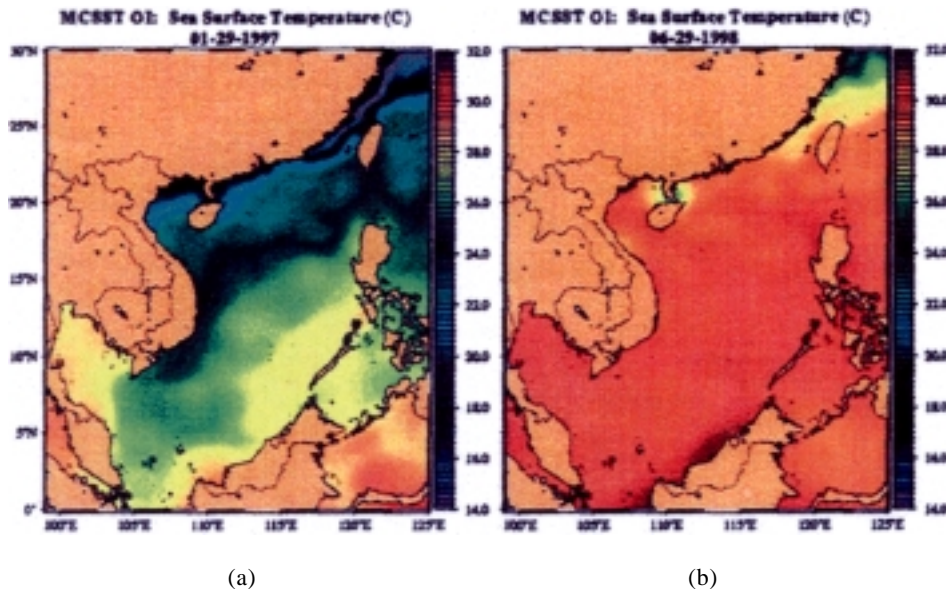


Fig. 2. NASA's multi-channel sea surface temperature (MCSST) data for (a) January 29, 1997, and (b) June 29, 1998. The data were interpolated by the Naval Research Laboratory.

of it. The maximum absolute values of the cyclonic curl (northwest side) and anticyclonic curl (southeast side) are  $1.8 \times 10^{-7} \text{ N/m}^3$  and  $10^{-7} \text{ N/m}^3$ , respectively. The strength of the wind stress curl during the summer monsoon season is about half that during the winter monsoon season. This implies a weak northeastward surface jet located at the zero-curl line.

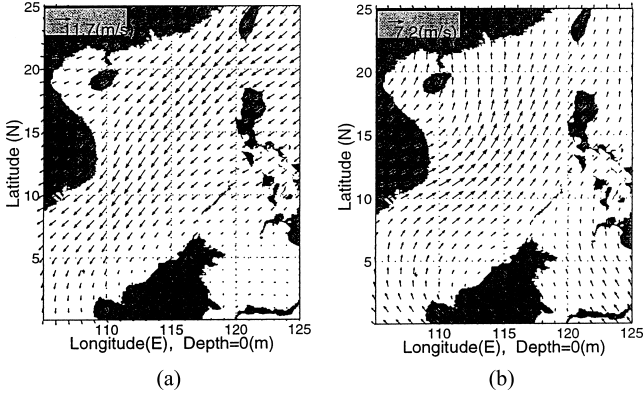


Fig. 3. Mean surface wind stress vectors in the South China Sea for (a) December and (b) June (after Chu *et al.*, 1997b).

### 3. The Navy's GDEM Data Set

GDEM is the Navy's global climatological monthly mean temperature and salinity data set with a four-dimensional (latitude, longitude, depth, and month) display. Data for building the current version of GDEM climatology for the SCS were obtained from the Navy's Master Oceanographic Observational Data Set (MOODS), which has 144,135 temperature and 13,768 salinity profiles during 1930–1997. The main limitation of the MOODS data is its irregular distribution in time and space. Certain periods and areas are over sampled while others lack enough observations to gain any meaningful insights. Vertical resolution and data quality are also highly variable depending to a great degree on instrument type and sampling expertise.

The basic design concept of GDEM is the determination of a set of analytical curves that represent the mean vertical distributions of temperature and salinity for grid cells ( $0.5^\circ \times 0.5^\circ$ ) through the averaging of the coefficients for the curves found for individual profiles (Teague *et al.*, 1990). Different families of representative curves have been chosen for shallow, mid-depth, and deep-depth ranges, with each chosen so that the number of parameters required to yield a smooth, mean profile over the range was minimized. As pointed by Teague *et al.* (1990),

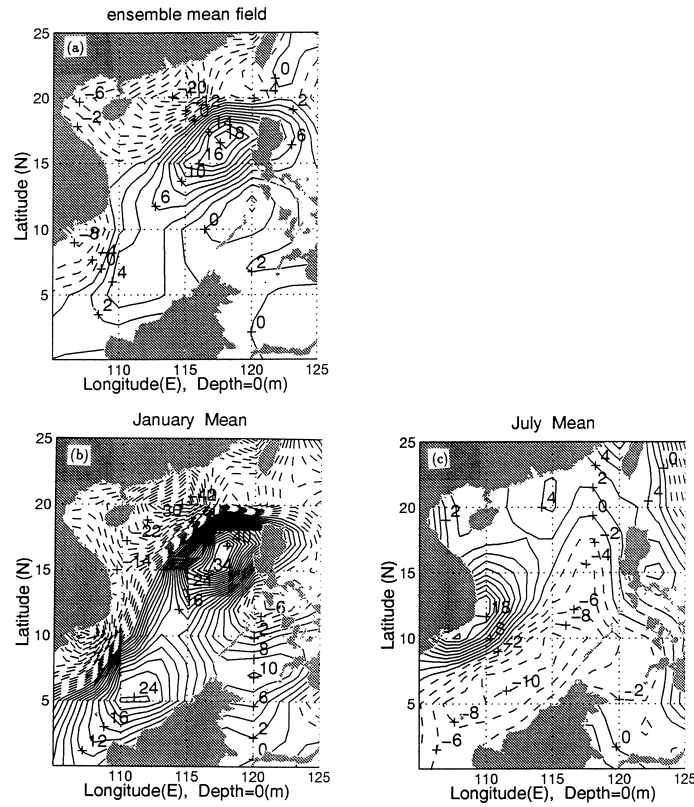


Fig. 4. Surface wind stress curl: (a) ensemble mean, (b) January, and (c) July. The unit is  $10^{-8} \text{ N m}^{-3}$  (after Chu *et al.*, 1997b).



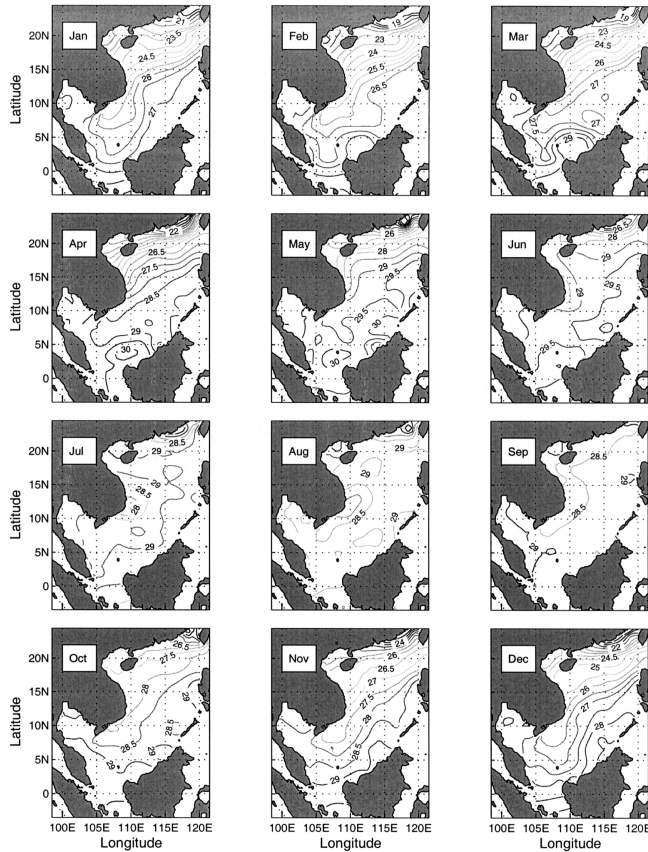


Fig. 5. Monthly mean sea surface temperature ( $^{\circ}\text{C}$ ) field with  $0.5^{\circ}\text{C}$  contour interval.

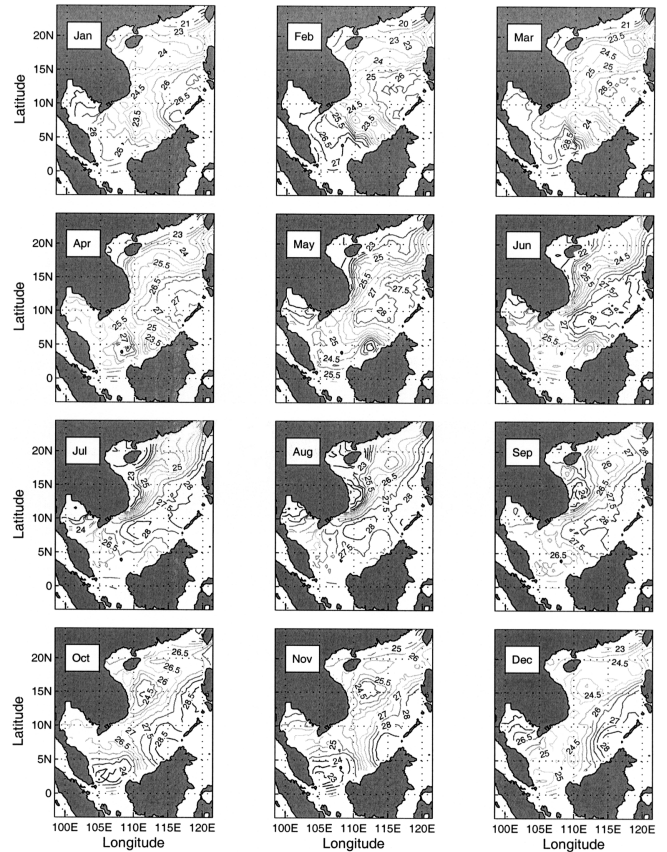


Fig. 6. Monthly mean temperature ( $^{\circ}\text{C}$ ) field at 50 m depth with  $0.5^{\circ}\text{C}$  contour interval.

large-scale oceanographic features are generally found to be similarly represented in both GDEM and the NOAA Climatological Atlas of the World Ocean temperature and salinity. GDEM appears to render better representations of seasonal variability and regions of high current shear because of a different smoothing method and a finer grid spacing. GDEM data contains the monthly mean temperature and salinity ( $T$ ,  $S$ ) and annual mean temperature and salinity ( $\bar{T}$ ,  $\bar{S}$ ) fields. Interested readers are referred to Teague *et al.* (1990) for more information.

#### 4. Thermohaline Front

The sea surface temperature (SST) variation obtained from the GDEM data is quite consistent with earlier investigations based on the National Center for Environmental Predictions (NCEP) data (Chu *et al.*, 1997b) and based on the MOODS data (Chu *et al.*, 1997a, 1999). An important feature, yet to be explored, is the thermohaline front (THF) across the SCS basin from Vietnam Bight ( $109^{\circ}\text{E}$ ,  $10^{\circ}\text{N}$ ) to the northwestern tip of Luzon ( $120^{\circ}\text{E}$ ,  $19^{\circ}\text{N}$ ).

#### 4.1 Temperature

Figure 5 shows the monthly mean sea surface temperature with contour interval of  $0.5^{\circ}\text{C}$ . The horizontal gradient across THF strengthens in the winter monsoon season (November to April) with a maximum value of  $1.4^{\circ}\text{C}/100\text{ km}$  and weakens drastically in the summer monsoon seas (June to September) (Fig. 5).

Figure 6 shows the monthly mean temperature at 50 m depth. Different from the surface, the temperature gradient is evident all year round. Moreover, we can see the seasonal variability of the multi-eddy structure in SCS which was reported by Chu and Chang (1997) and Chu *et al.* (1997a, 1997b, 1998).

#### 4.2 Salinity

Figure 7 shows the monthly mean surface salinity with contour interval of 0.25 ppt. The isoline of 33.75 ppt (or 33.5 ppt) in February to April (or May to January) divides the SCS into saltier northwestern SCS and fresher southeastern SCS. The horizontal salinity gradient across THF in the winter is comparable to that in the summer

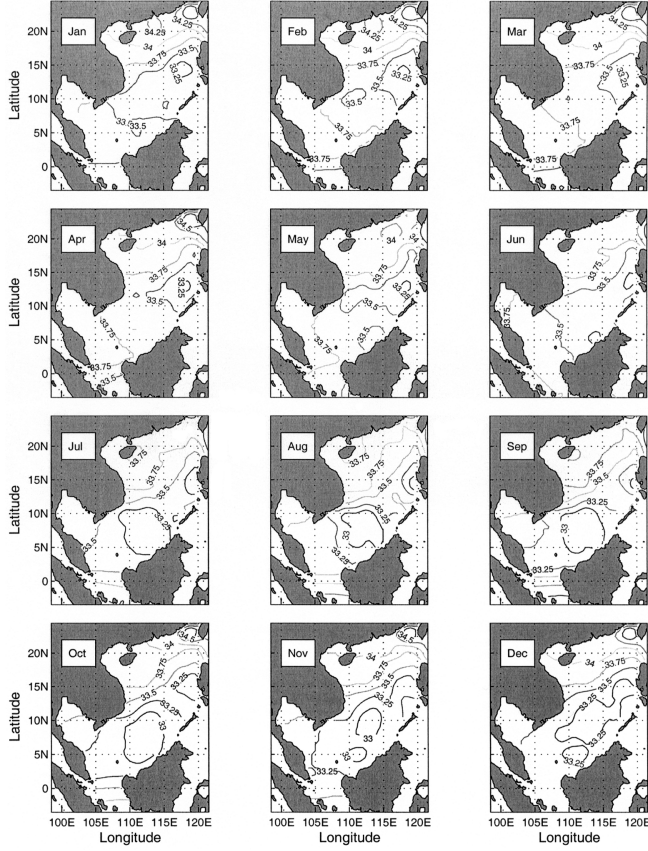


Fig. 7. Monthly mean sea surface salinity (ppt) field with 0.025 ppt contour interval.

(nearly 0.25 ppt/100 km). Figure 8 shows the monthly mean salinity at 50 m depth. The 34.0 ppt isoline separates the saltier, northwestern SCS from the fresher, southeastern SCS. A strong horizontal salinity gradient (0.1 ppt/100 km) is found near the Vietnam Bight in the summer monsoon season (July to October). THF appears strong all year round at the surface and subsurface (50 m).

### 4.3 Forcing mechanism

#### 4.3.1 Pre-conditioning

The SCS is occupied by two separate water masses. In the north, the waters are cold and saline. The annual variability of salinity is small, due to the inflow and diffusion of high salinity water from the Pacific Ocean through Luzon Strait. However, in the south the tropical conditions cause the waters to be warmer and fresher (Wyrtki, 1961). High temperature, low salinity water in the south and low temperature, high salinity water in the north is the pre-condition for the THF formation in the central SCS.

#### 4.3.2 Sverdrup transport

For the ensemble mean (Fig. 4(a)) and winter (Fig.

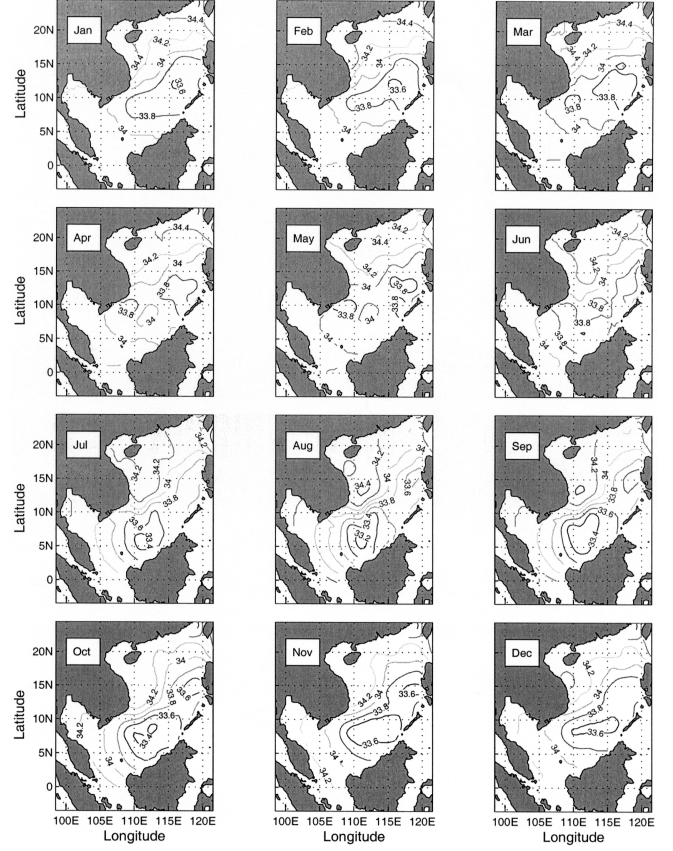


Fig. 8. Monthly mean salinity (ppt) field at 50 m depth with 0.02 ppt contour interval.

4(b))  $\zeta$  fields, the northeast-to-southwest oriented zero-curl line separates the SCS into anticyclonic curls (causing southward Sverdrup transport) northwest of it and cyclonic curls (causing northward Sverdrup transport) southeast of it. This process forces the two water masses to converge at the zero-curl line, causing the THF formation and/or strengthening the THF. For the summer (Fig. 4(b))  $\zeta$  field, the zero-curl line separates the SCS into cyclonic curls (causing northward Sverdrup transport) northwest of it and anticyclonic curls (causing southward Sverdrup transport) southeast of it. This process forces the two water masses to divergence at the zero-curl line, weakening the THF. Use of the Sverdrup theory also predicts the existence of a jet-like flow associated with the zero-curl line.

## 5. Cross-Basin Current

### 5.1 Flow pattern

Wyrtki (1961) published an overview of SCS seasonal surface circulations and postulated a cross-basin current (CBC) flowing northeastward all year round. A

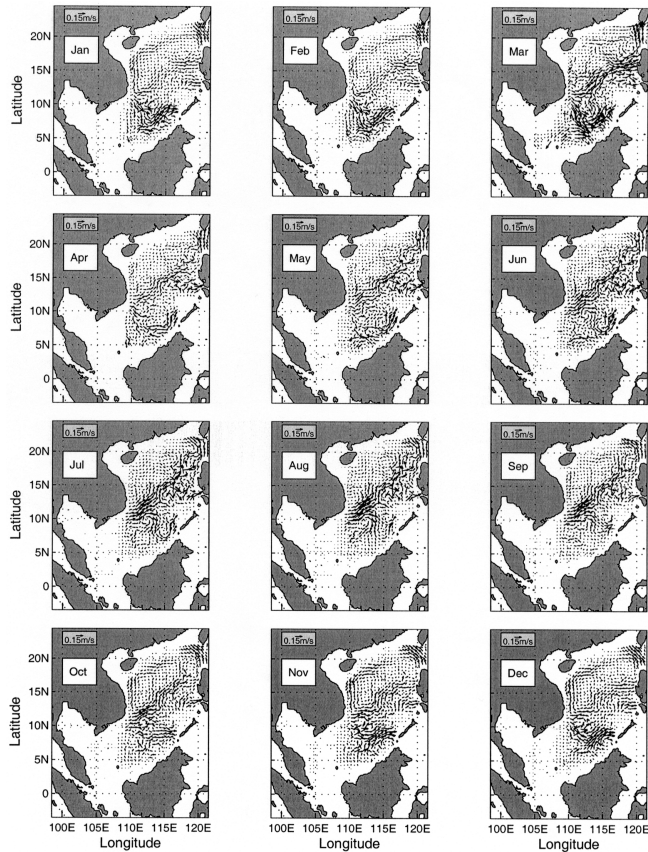


Fig. 9. Inverted monthly mean velocity field at the surface.

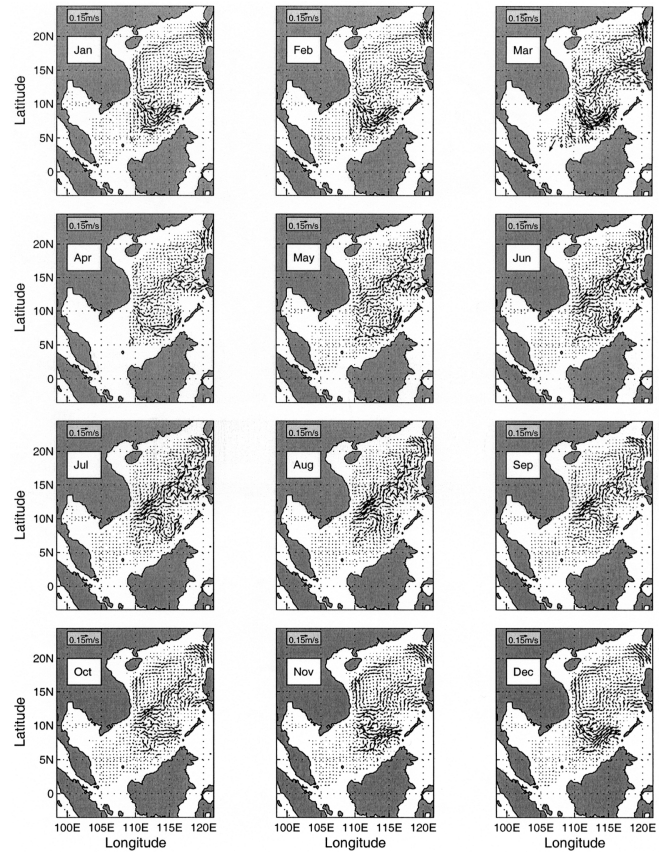


Fig. 10. Inverted monthly mean velocity field at 50 m depth.

wind-driven circulation is formed with the beginning of the southwest monsoon in May and June. Off the coast of Vietnam a northward flowing western boundary current is clearly visible. The wide, uniform drift in the northern SCS shows a deflection of the current to the right of the wind and forms CBC from the Vietnam bight to Luzon island. In September the strength of the currents decreases and in October the northeast monsoon starts blowing with considerable strength. Under the influence of the winds, water masses of the North Equatorial Current are intruded through Luzon Strait into SCS. This water flows along the coast of China to the southwest with a remarkable westward intensification of the current. In the central SCS a counter current (i.e., CBC) is developed north of 10°N.

The P-vector inverse method (Chu, 1995, 2000; Chu *et al.*, 1998; Chu and Li, 2000) was used to compute 3D absolute velocity from temperature and salinity data. The optimization scheme proposed by Chu *et al.* (1998) was also used to minimize errors. The calculated absolute velocity field (Figs. 9 and 10) clearly shows the existence of CBC flowing northeastward from the Vietnam bight to Luzon island. Different from Wyrki's cartoons,

the coastal currents are not well obtained using the P-vector method. A comparison of Figs. 9 and 10 with Figs. 5–8 shows the co-location of CBC and THF.

CBC has a weak seasonal variation in flow direction and a strong seasonal variation in current speed. It strengthens in the summer and weakens in the winter. In July and August, the maximum speed of CBC reaches  $0.25 \text{ m s}^{-1}$  ( $0.2 \text{ m s}^{-1}$ ) in the southern part near the Vietnam bight at the surface (50 m depth). In January and February CBC becomes very weak, around  $0.05 \text{ m s}^{-1}$  at the surface and 50 m deep. The seasonal variation of CBC was well reproduced by numerical modeling (e.g., Chu *et al.*, 1999).

CBC meanders and generates cyclonic (anticyclonic) eddies to the northwest (southeast). For example, CBC meanders at (110°E, 10°N) from June to August. An anticyclonic eddy has been identified with its center at (112°E, 9°N) and a size of around 300 km. The tangential velocity of this eddy is nearly  $0.2 \text{ m s}^{-1}$ . The multi-eddy structure inverted here is consistent with early calculations on the  $z$ -level using synoptic data (Chu *et al.*, 1998) and on the isopycnal level using GDEM (Chu and Li, 2000). The

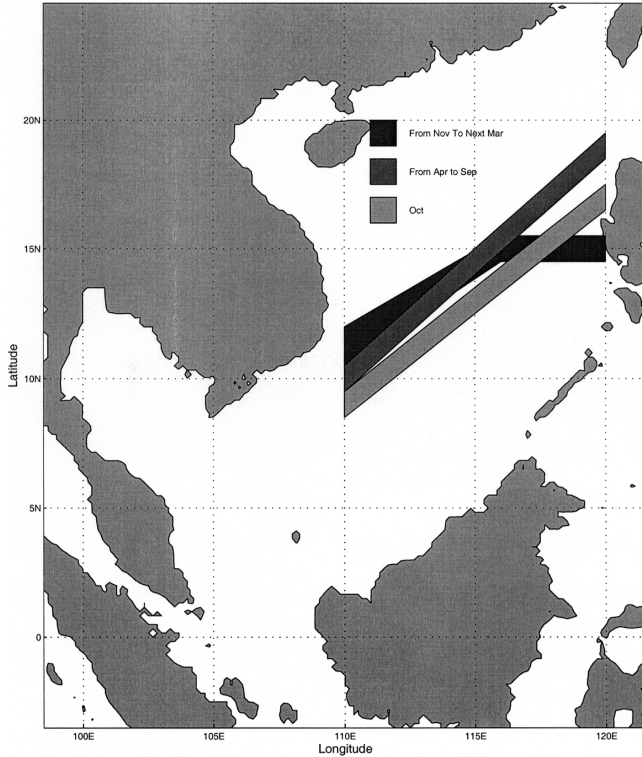


Fig. 11. Seasonal variation of the CBC axis at 50 m depth.

multi-eddy structure has been reproduced by numerical simulations (e.g., Chu *et al.*, 1999).

### 5.2 Axis of the cross-basin current

The orientation of the maximum velocity along CBC is defined as the axis that extends from (110°E, 10°N) to (120°E, 18°N) in a straight line at 50 m depth (as an example) from April to September (Fig. 11). In October, the axis maintains as a straight line course and shifts southward with a larger displacement in the northern part (250 km in the north tip) than in the southern part (100 km in the south tip). From November to March, the CBC axis is no longer a straight line. The western part of the axis (west of 115°E) jumps around 200 km northward compared to October. The eastern part (east of 115°E) of the axis becomes zonal along 15°N latitude.

## 6. Water Mass Characteristics across the Front

### 6.1 Sub-areas

As described in Subsection 4.3.1, the water masses have different characteristics north and south of THF, with high temperature, low salinity water in the south and low temperature, high salinity water in the north. Analysis of  $T$ ,  $S$  data in the latitudinal strip (112.5°–115°E) is necessary to quantify the thermohaline variability across THF

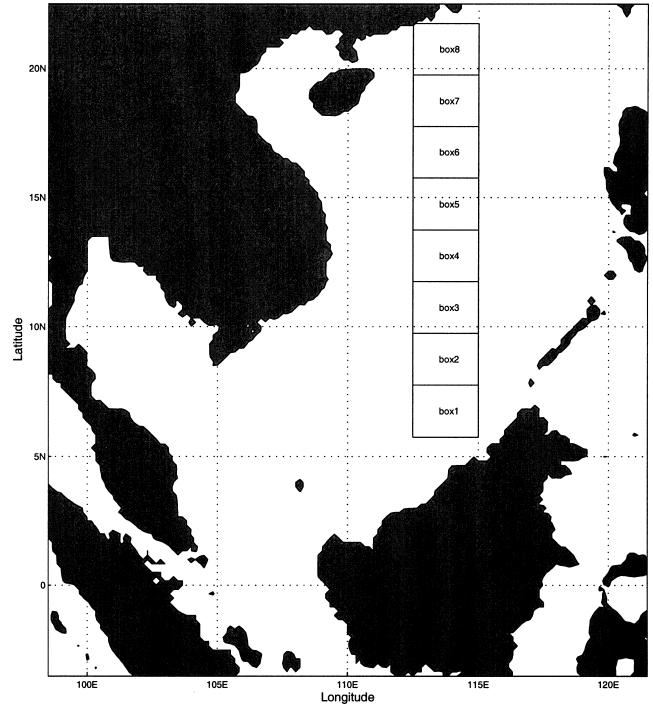


Fig. 12. Division of subareas across THF.

and for a further understanding of the driving and variation mechanism of THF. This strip is divided from 6° to 22°N into eight rectangles with 2.5° in zonal direction and 2° in latitudinal direction (Fig. 12). These boxes can be grouped into three sub-areas: THF (4 and 5), south of THF (1–3), and north of THF (6–8). The change of  $T$ - $S$  features among these boxes leads to an understanding of the THF structure and the forcing mechanism.

### 6.2 $T$ - $S$ diagrams

We have plotted the upper layer (0–300 m deep)  $T$ - $S$  diagrams for each box in January (Fig. 13) and July (Fig. 14), respectively. The  $T$ - $S$  curves in all boxes are of the same type (reverse-C shape) with a salinity maximum (nearly 34.65 ppt north of THF and around 34.52 ppt south of THF) layer. The maximum salinity has been previously discussed by Qu (2000) using  $T$ ,  $S$  profiles from the National Ocean Data Center (NODC). The location and the strength of the maximum salinity are comparable whether they are studied using the GDEM (this paper) or NODC data (Qu, 2000).

The  $T$ - $S$  curves, however, have a larger range in both  $T$  and  $S$  south of THF (Boxes 1–3) than to the north (Boxes 6–8), and the salinity maximum occurs at a shallower depth north of THF ( $\sigma_t \approx 25$  in Boxes 6 and 7) than to the south ( $\sigma_t \approx 25.6$ – $25.8$  in Boxes 1–3). Thus, the thermohaline variability is larger to the south than to the north of THF.

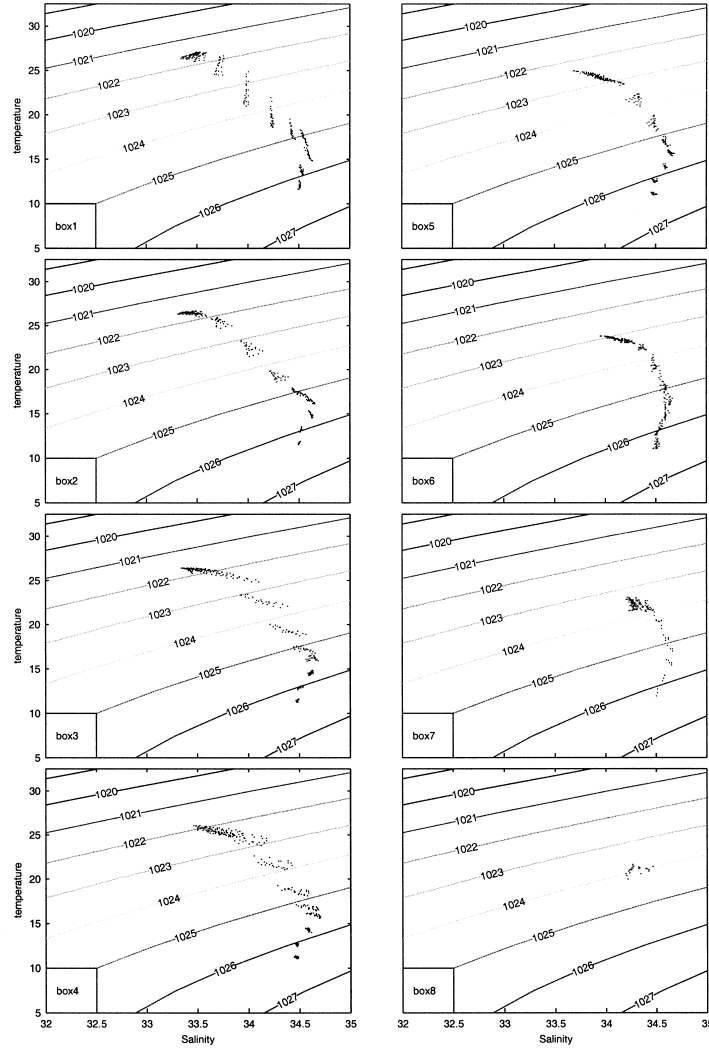


Fig. 13. Change of T-S diagrams across THF in January.

### 6.3 T-S profiles

We have plotted the mean vertical  $T$ - $S$  profiles for each box in January (Fig. 15) and July (Fig. 16), respectively. The thermohaline structure below 150 m is quite uniform horizontally and has weak seasonal variability between January and July, which indicates that THF is an upper layer phenomenon. The halocline is stronger south of THF than to the north in both seasons (January and July). For example, the vertical salinity gradient in January is around 0.83 ppt/100 m in Box 2 (south of THF) and nearly 0.38 ppt/100 m in Box 6 (north of THF), and the vertical salinity gradient in July is around 0.92 ppt/100 m in Box 2 (south of THF) and nearly 0.56 ppt/100 m in Box 6 (north of THF). The salinity maximum ( $\sim 34.65$  ppt) occurs at shallower depth north of THF (around 150 m deep in Boxes 6 and 7) than to the south (around 200 m deep in Boxes 1–3). There is no noticeable seasonal vari-

ability.

Seasonal thermohaline variability is evident above 150 m depth, and is stronger north of THF than to the south. For example, January temperature profiles (Fig. 15) show deeper mixed layers north of THF (e.g., around 60 m in Box 6) than to the south (e.g., 35 m in Box 2). This is caused by the dipole of the surface wind stress curl with anticyclonic curl north of THF and cyclonic curl to the south. July temperature profiles (Fig. 16) show shallower mixed layers north of THF (e.g., around 10 m in Box 6) than to the south (e.g., 30 m in Box 2) with the same mechanism as January.

### 6.4 Surface temperature

Monthly mean SST data show a larger seasonal variability to the north (Box-6) than south (Box-2) of THF (Figs. 17(a) and 17(b)). The coldest SST occurs in Feb-

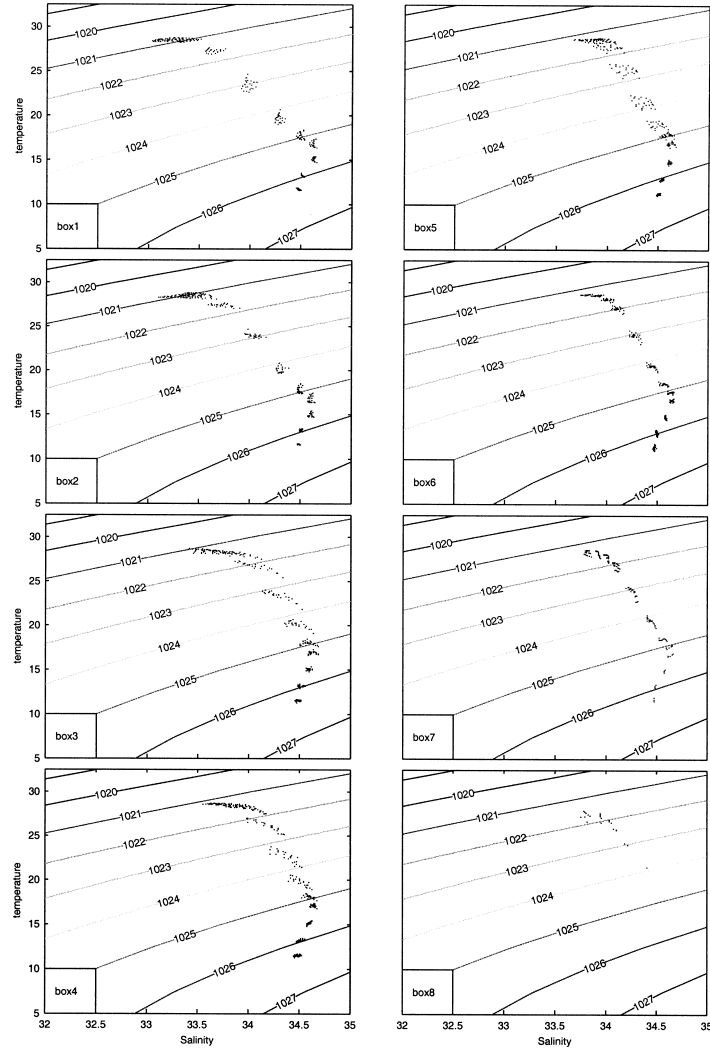


Fig. 14. Change of T-S diagrams across THF in July.

ruary in both boxes: 23.5°C in Box-6 (north of THF), and 26.6°C in Box-2 (south of THF). The warmest SST north (south) of THF is 29.1°C (29.6°C) appearing in July (May). The seasonal variability (warmest minus coldest temperature) is around 5.6°C in Box-6 and 3°C in Box-2.

We use the SST difference between Box-2 and Box-6 ( $\Delta\text{SST} = \text{SST}_{\text{Box-2}} - \text{SST}_{\text{Box-6}}$ ) to represent the strength of the surface THF in temperature (Fig. 17(c)). The difference  $\Delta\text{SST}$  reaches a maximum value (3.1°C, strongest surface THF) in January, and a minimum value of -0.2°C in July and August (no surface THF).

#### 6.5 Subsurface (50 m) temperature

Monthly mean temperature at 50 m depth shows a larger seasonal variability north (Box-6) of than south (Box-2) of THF (Figs. 18(a) and 18(b)). The coldest temperature occurs in February in both boxes: 23.3°C in Box-

6 (north of THF), and 25.5°C in Box-2 (south of THF). The warmest temperature north (south) of THF is 26.8°C (27.8°C) appearing in October (June). The seasonal variability is around 3.5°C in Box-6 and 2.3°C in Box-2.

We use the temperature difference between Box-2 and Box-6 ( $\Delta T = T_{\text{Box-2}} - T_{\text{Box-6}}$ ) to represent the strength of the THF (Fig. 18(c)) at 50 m depth. The difference  $\Delta T$  is larger in summer than in winter, and reaches 3.6°C (strongest subsurface THF) in June, and 0.9°C in October (weak subsurface THF).

#### 6.6 Surface salinity

Monthly mean surface salinity shows different seasonal variabilities north (Box-6) and south (Box-2) of THF (Figs. 19(a) and 19(b)). Low salinity is 33.78 ppt (32.96 ppt) north (south) of THF appearing in July and August (October and November). High salinity is 34.14 ppt (33.57

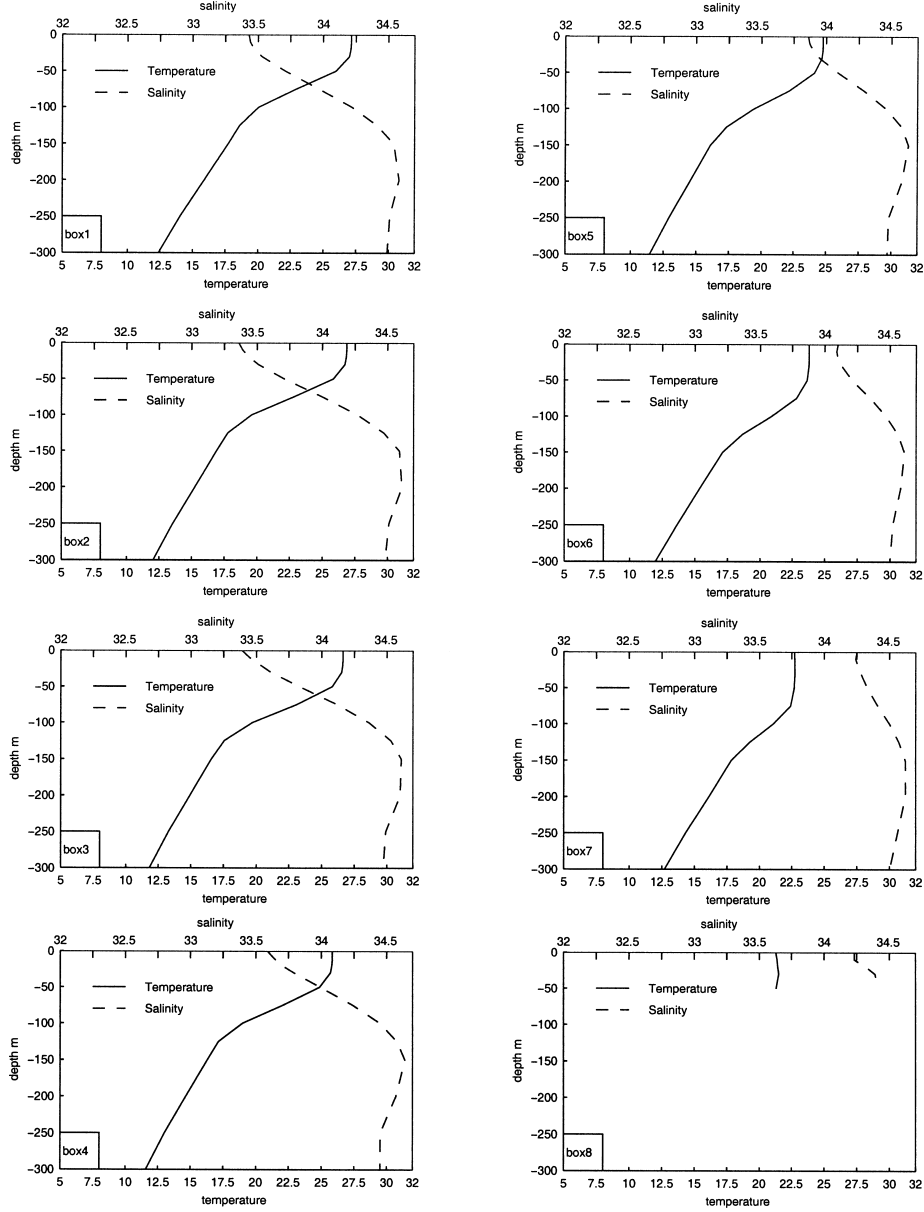


Fig. 15. Change of T and S profiles across THF in January.

ppt) north (south) of THF appearing in February (March). The seasonal variability is around 0.61 ppt (0.36 ppt) north (south) of THF.

We use the salinity difference between Box-2 and Box-6 ( $\Delta S = S_{\text{Box-2}} - S_{\text{Box-6}}$ ) to represent the strength of the surface THF in salinity (Fig. 19(c)). The values of  $\Delta S$  are all negative, indicating that the surface water is more saline to the north than south of THF. The difference  $|\Delta S|$  reaches a maximum value (0.96 ppt, strongest surface THF in salinity) in November, and a minimum value of 0.4 ppt in May (weak surface THF in salinity). The sea-

sonal variation of  $|\Delta S|$  is mainly caused by the salinity decrease in the southern portion of SCS (Fig. 19(b)). This confirms that the major mechanism for the THF formation is the local expansion-blocking mechanism described in Section 4.

#### 6.7 Subsurface (50 m) salinity

Monthly mean salinity values at 50 m depth show a nearly in-phase seasonal variability north (Box-6) and south (Box-2) of THF (Figs. 20(a) and 20(b)). The minimum salinity north (south) of THF is 34.14 ppt (33.64



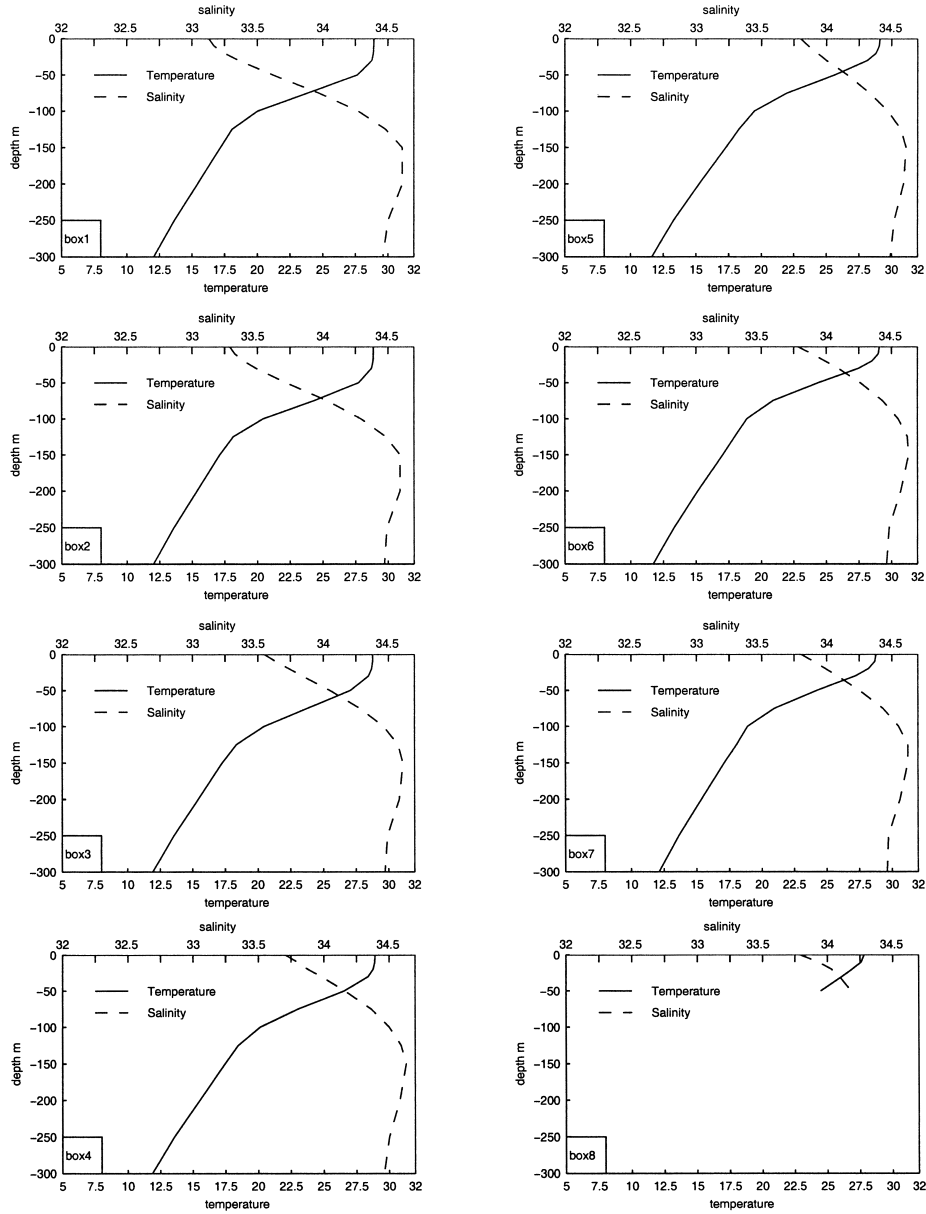


Fig. 16. Change of T and S profiles across THF in July.

ppt) appearing in November (August and September). The maximum salinity occurs in May: 34.36 ppt north of THF, and 33.87 ppt south of THF. The seasonal variability is around 0.22 ppt in Box-6 and 0.23 ppt in Box-2, representing comparable seasonal variabilities north and south of THF.

The salinity difference between Box-2 and Box-6 (Fig. 20(c)) represents the strength of the subsurface THF in salinity. The values of  $\Delta S$  are all negative, indicating that the subsurface water is more saline to the north than south of THF. The difference  $|\Delta S|$  is nearly 0.5 ppt all year round.

## 7. Conclusions

(1) Using the Navy's open domain Generalized Digital Environmental Model (GDEM) climatological temperature and salinity data on a  $0.5^\circ \times 0.5^\circ$  grid, an upper layer THF across the South China Sea (SCS) from the South Vietnam coast (around  $15^\circ\text{N}$ ) to Luzon Island (around  $19^\circ\text{N}$ ) has been identified. Its axis is along the line between two points ( $110^\circ\text{E}$ ,  $10^\circ\text{N}$ ) and ( $120^\circ\text{E}$ ,  $19^\circ\text{N}$ ). Vertical thermohaline variability is larger to the south than north of this front. The halocline is stronger south of the THF than to the north. The vertical salinity gradient is around 0.83 ppt/100 m (0.92 ppt/100 m) south of THF

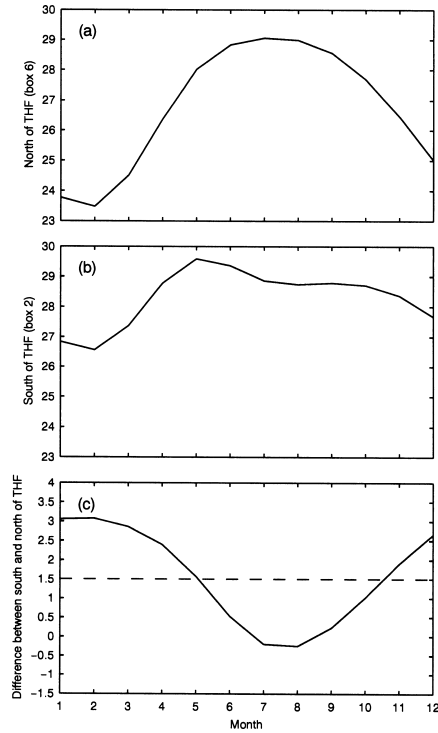


Fig. 17. Monthly evolutions of (a) SST (°C) north of THF (Box-6), (b) SST (°C) south of THF (Box-2), and (c) the difference between the two ( $\Delta$ SST). A criterion of  $\Delta$ SST = 1.5°C (denoted by the dashed line) is used to represent the occurrence of THF. If  $\Delta$ SST  $\leq$  1.5°C, the temperature difference is not evident across THF.

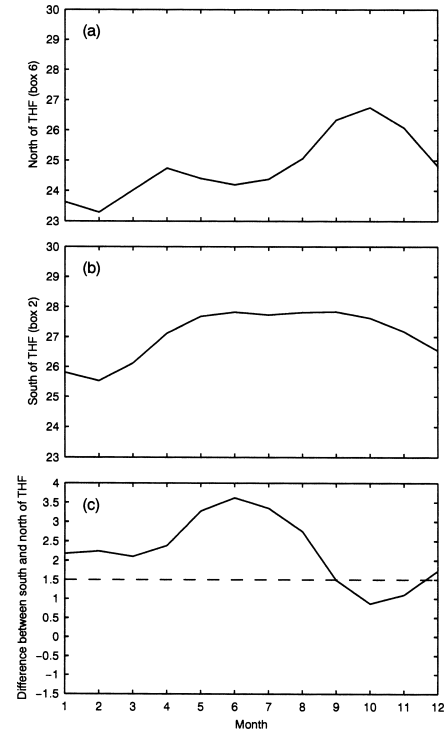


Fig. 18. Monthly evolutions at 50 m depth of (a) temperature (°C) north of THF (Box-6), (b) temperature (°C) south of THF (Box-2), and (c) the difference between the two ( $\Delta$ T). A criterion of  $\Delta$ T = 1.5°C (denoted by the dashed line) is used to represent the occurrence of THF. If  $\Delta$ T  $\leq$  1.5°C, the temperature difference is not evident across THF.

and nearly 0.38 ppt/100 m (0.56 ppt/100 m) north of THF in January (July). The location and the strength of the maximum salinity have been found to be comparable using the GDEM and NODC (Qu, 2000) data. The GDEM data show that the salinity maximum (~34.65 ppt) occurs at shallower depth north of THF (around 150 m) than to the south (around 200 m).

(2) Seasonal thermal variability is stronger north of THF than to the south. The seasonal variability at the surface is around 5.6°C north of THF and 3°C to the south. The seasonal variability at 50 m depth is around 3.5°C north of THF and 2.3°C to the south. In the summer, the horizontal temperature gradient across THF is not evident at the surface but it is evident at the sub-surface (50 m). In the winter, the temperature gradient is evident at both surface and subsurface. At the subsurface (50 m depth), a maximum horizontal temperature gradient (1.4°C/100 km) is found near the Vietnam Bight.

(3) Seasonal haline variability changes with depth. At the surface there is a phase shift between north and south of THF. Low salinity is 33.78 ppt (32.96 ppt) north (south) of THF appearing in July and August (October

and November). High salinity is 34.14 ppt (33.57 ppt) north (south) of THF appearing in February (March). The seasonal variability is around 0.61 ppt (0.36 ppt) north (south) of THF. The salinity gradient across THF is strongest in November, and weakest in May.

At the subsurface (50 m deep), the seasonal haline variability is in-phase between north and south of THF. Low salinity is 34.14 ppt (33.64 ppt) north (south) of THF appearing in October (September and October). High salinity occurs in May: 34.36 ppt north of THF and 33.87 ppt to the south. The seasonal variability is around 0.22 ppt north of THF and 0.23 ppt to the south representing comparable seasonal variabilities north and south of THF.

(4) Deeper mixed layers are found to the north of than south of THF in the winter monsoon season (January) and vice versa in the summer monsoon season (July). This is caused by the dipole of the surface wind stress curl with anticyclonic curl north of THF and a cyclonic curl to the south in January and vice versa in July.

(5) An upper-layer, northeastward-flowing cross-basin current has been identified from GDEM data using the P-vector method. This coincides with the classical

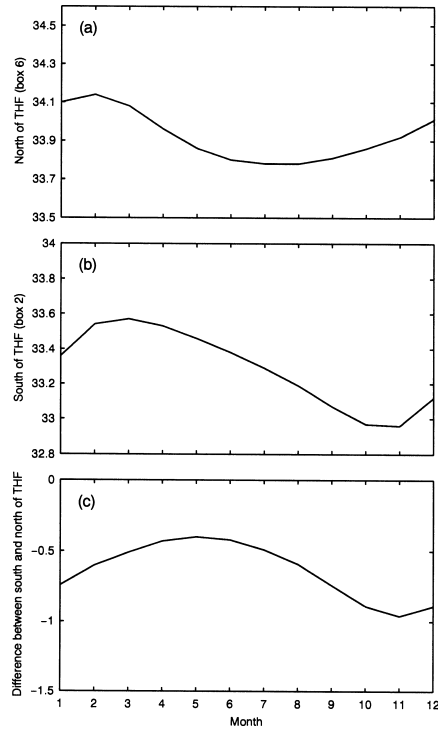


Fig. 19. Monthly evolutions at the surface of (a) salinity (ppt) north of THF (Box-6), (b) salinity (ppt) south of THF (Box-2), and (c) the difference between the two ( $\Delta S$ ).

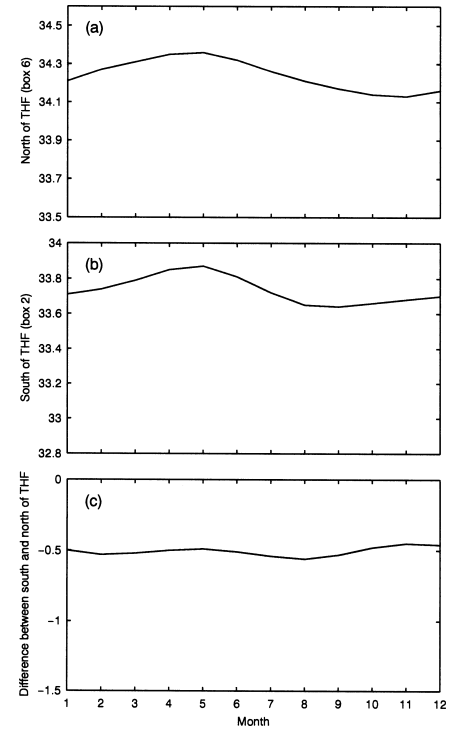


Fig. 20. Monthly evolutions at 50 m depth of (a) salinity (ppt) north of THF (Box-6), (b) salinity (ppt) south of THF (Box-2), and (c) the difference between the two ( $\Delta S$ ).

surface circulation pattern presented by Wyrski (1961). This current, flowing along THF from the Vietnam Bight to Luzon Island, has a weak seasonal variation in direction and a strong seasonal variation in current speed. It strengthens in the summer and weakens in the winter. In July and August, the maximum speed of CBC reaches  $0.25 \text{ m s}^{-1}$  ( $0.2 \text{ m s}^{-1}$ ) in the southern part near the Vietnam bight at the surface (50 m depth). In January and February CBC becomes very weak, around  $0.05 \text{ m s}^{-1}$  at the surface and 50 m deep. CBC meanders and generates cyclonic (anticyclonic) eddies northwest (southeast) of it.

(6) A local mechanism of water mass expansion-blocking due to the surface wind stress (jet and curl) has been proposed to explain the formation of THF. The anticyclonic curls cause the expansion of the cold and saline northwestern SCS water during the winter monsoon season and the expansion of the warm and fresher southeastern SCS water during the summer monsoon season (water mass expansion mechanism). The expansion is stopped by the northeast-southwest oriented atmospheric surface jet across SCS (water mass blocking mechanism). This mechanism can explain the formation of THF and the collocation of THF and the atmospheric surface jet. We plan to test this mechanism using a realistic ocean model.

## References

- Chao, S. Y., P. T. Shaw and J. Wang (1996): Deep water ventilation in the South China Sea. *Deep-Sea Res.*, **43**, 445–466.
- Chu, P. C. (1995): P vector method for determining absolute velocity from hydrographic data. *Mar. Technol. Soc. J.*, **29**(3), 3–14.
- Chu, P. C. (2000): P-vector spirals and determination of absolute velocities. *J. Oceanogr.*, **56**, 591–599.
- Chu, P. C. and C.-P. Chang (1997): South China Sea warm pool in boreal spring. *Adv. Atmos. Sci.*, **14**, 195–206.
- Chu, P. C. and R. F. Li (2000): South China Sea isopycnal surface circulations. *J. Phys. Oceanogr.*, **30**, 2419–2438.
- Chu, P. C., H. C. Tseng, C. P. Chang and J. M. Chen (1997a): South China Sea warm pool detected in spring from the Navy's Master Oceanographic Observational Data Set (MOODS). *J. Geophys. Res.*, **102**, 15761–15771.
- Chu, P. C., S. H. Lu and Y. C. Chen (1997b): Temporal and spatial variabilities of the South China Sea surface temperature anomaly. *J. Geophys. Res.*, **102**, 20937–20955.
- Chu, P. C., C. W. Fan, C. J. Lozano and J. Kerling (1998): An airborne expandable bathythermograph (AXBT) survey of the South China Sea, May 1995. *J. Geophys. Res.*, **103**, 21637–21652.
- Chu, P. C., N. L. Edmons and C. W. Fan (1999): Dynamical mechanisms for the South China Sea seasonal circulation and thermohaline variabilities. *J. Phys. Oceanogr.*, **29**, 2971–2989.

- Li, L., W. D. Nowlin, Jr. and J. Su (1998): Anticyclonic rings from the Kuroshio in the South China Sea. *Deep-Sea Res. I*, **45**, 1469–1482.
- Metzger, E. J. and H. E. Hurlburt (1996): Coupled dynamics of the South China Sea, the Sulu Sea, and the Pacific Ocean. *J. Geophys. Res.*, **101**, 12331–12352.
- Metzger, E. J. and H. E. Hurlburt (2001): The nondeterministic nature of Kuroshio penetration and eddy shedding in the South China Sea. *J. Phys. Oceanogr.*, **31**, 1712–1731.
- Nitani, H. (1970): Oceanographic conditions in the sea east of Philippines and Luzon Strait in summer of 1965 and 1966. p. 213–232. In *The Kuroshio—A Symposium on Japan Current*, ed. by J. D. Marr, East-West Press, Honolulu, Hawaii.
- Qu, T. D. (2000): Upper layer circulation in the South China Sea. *J. Phys. Oceanogr.*, **30**, 1450–1460.
- Shaw, P. T. (1989): The intrusion of water masses into the sea southwest of Taiwan. *J. Geophys. Res.*, **94**, 18213–18226.
- Shaw, P. T. (1991): The seasonal variation of the intrusion of the Philippine Sea water into the South China Sea. *J. Geophys. Res.*, **96**, 821–827.
- Teague, W. J., M. J. Carron and P. J. Hogan (1990): A comparison between the Generalized Digital Environmental Model and Levitus climatology. *J. Geophys. Res.*, **95**, 7167–7183.
- Wyrski, K. (1961): Scientific results of marine investigations of the South China Sea and the Gulf of Thailand 1959–1961. *Naga Report*, Vol. 2, University of California at San Diego, 195 pp.